Faculty Scholarship

2-20-2024

Effects Of Micromachining on Anti-Oxidant Elution From a Mechanically-Adaptive Polymer

Natalie N. Mueller
Case Western Reserve University, nnm19@case.edu

Youjoung Kim
Case Western Reserve University, yjk14@case.edu

Mali Ya Mungu Ocoko
Case Western Reserve University, mlo38@case.edu

Peter Dernelle
Case Western Reserve University

Ishani Kale
Case Western Reserve University

See next page for additional authors

Follow this and additional works at: https://commons.case.edu/facultyworks

Recommended Citation

Authors

Natalie N. Mueller, Youjoung Kim, Mali Ya Mungu Ocoko, Peter Dernelle, Ishani Kale, Simran Patwa, Anna Clarissa Hermoso, Deeksha Chirra, Jeffrey R. Capadona, and Allison E. Hess-Dunning

Effects of micromachining on anti-oxidant elution from a mechanically-adaptive polymer

Natalie N Mueller[1,2] ⓘ**, Youjoung Kim**[1,2]**, Mali Ya Mungu Ocoko**[1,2]**, Peter Dernelle**[1,2]**, Ishani Kale**[1,2]**, Simran Patwa**[1,2]**, Anna Clarissa Hermoso**[1,2]**, Deeksha Chirra**[1,2]**, Jeffrey R Capadona**[1,2] ⓘ **and Allison Hess-Dunning**[1,2,*] ⓘ

[1] Department of Biomedical Engineering, Case Western Reserve University, Cleveland, OH, United States of America
[2] Advanced Platform Technology Center, Louis Stokes Cleveland VA Medical Center, Cleveland, OH, United States of America

E-mail: aeh19@case.edu

CrossMark

Abstract

Intracortical microelectrodes (IMEs) can be used to restore motor and sensory function as a part of brain–computer interfaces in individuals with neuromusculoskeletal disorders. However, the neuroinflammatory response to IMEs can result in their premature failure, leading to reduced therapeutic efficacy. Mechanically-adaptive, resveratrol-eluting (MARE) neural probes target two mechanisms believed to contribute to the neuroinflammatory response by reducing the mechanical mismatch between the brain tissue and device, as well as locally delivering an antioxidant therapeutic. To create the mechanically-adaptive substrate, a dispersion, casting, and evaporation method is used, followed by a microfabrication process to integrate functional recording electrodes on the material. Resveratrol release experiments were completed to generate a resveratrol release profile and demonstrated that the MARE probes are capable of long-term controlled release. Additionally, our results showed that resveratrol can be degraded by laser-micromachining, an important consideration for future device fabrication. Finally, the electrodes were shown to have a suitable impedance for single-unit neural recording and could record single units *in vivo*.

Supplementary material for this article is available online

Keywords: neural interfaces, resveratrol, microelectrode fabrication, neuroinflammation

---

* Author to whom any correspondence should be addressed.

1. Introduction

Spinal cord injury and neurodegenerative disorders such as Parkinson's disease are debilitating neurological conditions that can result in loss of motor and sensory function, leading to a reduced quality of life [1–5]. Intracortical microelectrodes (IMEs), as part of a brain–computer interface system, can aid in restoring function through functional electrical stimulation [6–8]. In addition, IMEs facilitate in brain mapping and neuroscience research. Unfortunately, IMEs typically show reduced recording and stimulation performance over time, leading to failure within weeks to months after implantation [9–12]. Reduced performance and eventual failure can result in reduced therapeutic efficacy of the brain–computer interface system. Therefore, improving IME longevity *in vivo* is critical.

A primary mode of IME failure results from a chronic neuroinflammatory response following implantation of the device. Initial implantation causes vascular injury, compromising the blood–brain barrier and allowing macrophages, monocytes, and blood proteins to enter the brain [9, 13–16]. Additionally, resident immune cells of the brain, such as microglia and astrocytes, are activated and recruited to the implant site. Inflammatory-activated enzymatic reactions in reactive microglia and macrophages can generate increased concentrations of reactive oxygen species (ROS), leading to oxidative stress in the local tissue [17]. Oxidative stress can further perpetuate neuroinflammation by positive feedback, resulting in higher ROS concentrations [18, 19]. ROS can also cause oxidation and corrosion of the electrode contacts, as well as delamination of the insulation layer [20–22]. Furthermore, ROS can oxidize nucleic acids, lipids, and proteins, facilitating collateral cell death, especially in neurons [23, 24].

At a chronic time point, reactive astrocytes form a glial scar, walling off the implant site from the healthy brain tissue, including neurons [25]. Micromotion at the device-tissue interface can result in increased differential strain due to mechanical mismatch, further exacerbating the astrocytic scar around the implant [26–28]. As glial encapsulation occurs, the impedance of the tissue increases, while neurons are driven away or die off, making it increasingly difficult to record single units [29–31].

Utilizing techniques to target the oxidative stress and mechanical mismatch can help lead to improved IME integration [32]. Delivery of therapeutics with antioxidant and anti-inflammatory properties such as curcumin and resveratrol reduce oxidative stress and neuroinflammatory markers [33–40]. Additionally, compliant structural materials such as 'soft' polymers reduce mechanical mismatch and resulting neuroinflammation compared to stiff materials like silicon or glass [41–43]. Although employing local antioxidant delivery and compliant materials have shown improvement in the histological markers of neuroinflammation, their effect on recording performance has not been demonstrated, mainly due to microfabrication limitations.

Local drug delivery from implanted systems facilitates the delivery of the appropriate therapeutic dose directly to the target tissue. Local delivery also prevents side effects associated with systemic delivery, such as off-target effects, as well as metabolization and breakdown of the drug prior to reaching the site of action [44]. Therefore, local therapeutic delivery can translate to improved patient compliance and medication adherence as well as decreased discomfort [45].

Microfabrication techniques borrowed from the semiconductor industry such as photolithography and thin-film deposition have been used to advance the design and reproducibility of microscale devices for sensing, analysis, or control of the biological environment [46, 47]. Though drug-eluting devices have been explored for addressing the effects of the neuroinflammatory tissue responses to microfabricated implants [48, 49], the fabrication processes required for integrating electrical components (*e.g.*, sensors) onto a material impregnated with a therapeutic agent has not been reported.

In this work, we utilized a mechanically-adaptive polymer-based nanocomposite (NC) material that remains stiff during implantation, but becomes compliant in the brain due to the water content and physiological heat [50–54]. The NC was loaded with the antioxidant resveratrol for elution into the surrounding brain tissue when the NC is in its compliant state [33]. Functional recording electrodes were integrated on the substrate using microfabrication tools and techniques [55]. An overview of the mechanically-adaptive, resveratrol-eluting (MARE) neural probe system is shown in figure 1. Resveratrol release studies were completed to characterize the release profile and isomer. Finally, the MARE probes were implanted for up to 12 weeks to evaluate their ability to record single units *in vivo*.

2. Methods

2.1. Preparation of substrate

The polymer-based NC substrate for the neural probe is composed of polyvinyl acetate with 15% w/w tunicate cellulose nanocrystals (PVAc/t-CNC) and loaded with 0.01% w/w trans-resveratrol [50–54]. The mechanically-adaptive material was prepared using a film casting and evaporation method [42, 50–54], shown in figure 2. Briefly, polyvinyl acetate (Sigma-Aldrich, St. Louis, MO, USA), tunicate cellulose nanocrystals (Cellulose Lab, Fredericton, New Brunswick, Canada), and trans-resveratrol (Mega Resveratrol, Danbury, CT, USA) were separately dispersed in an organic solvent, dimethylformamide (DMF) (68-12-2, Fisher-Scientific, Hampton, New Hampshire, USA). The polyvinyl acetate and resveratrol solutions were placed on a stir plate until dissolved. The tunicate cellulose nanocrystal solution was placed in an ultrasonic bath (FS30, Fisher-Scientific, Hampton, New Hampshire, USA) of deionized water for 6 h or until the solution exhibits birefringence under cross-polarizers. The polyvinyl acetate, tunicate cellulose nanocrystal, and resveratrol solutions were then combined and stirred using a magnetic stir bar for 30 min. The homogenous solution was then cast in a low-form PTFE evaporating dish (Fisher-Scientific, Hampton, New Hampshire, USA) with a layer of Sylgard 184 silicone elastomer (PDMS) (Dow Chemical Company, Midland, Michigan, USA) coating
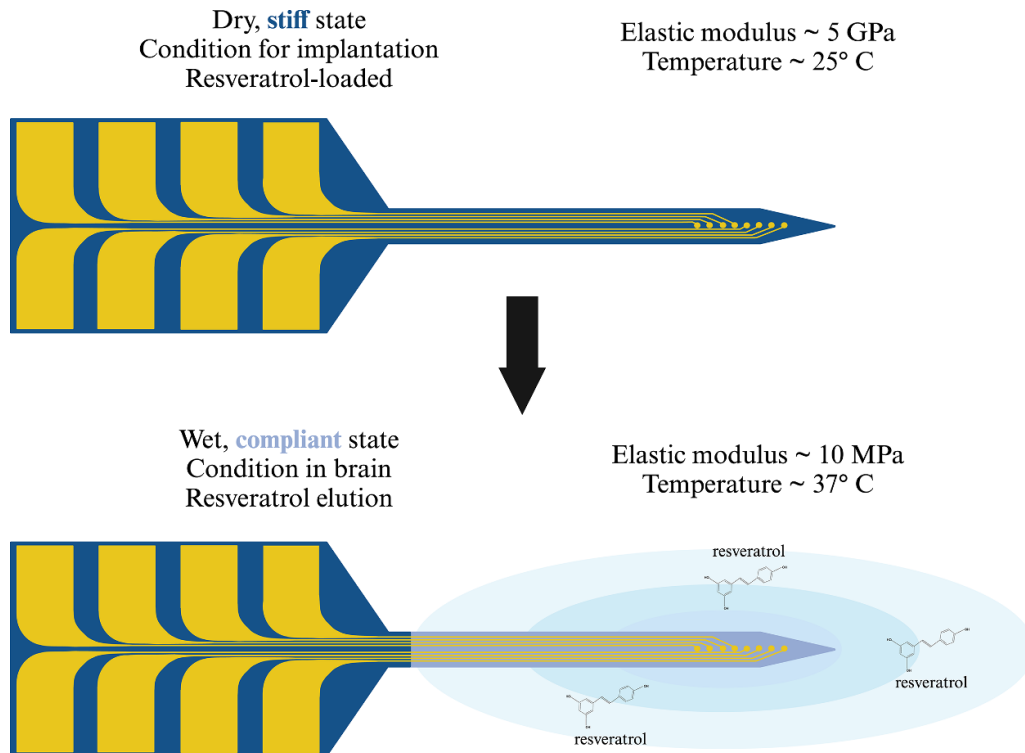
Figure 1. Overview of mechanically-adaptive, resveratrol-eluting (MARE) neural probes. The MARE probe is stiff when dry at 25 °C (room temperature), with a Young's modulus of 5 GPa. The stiffness of the substrate, reinforced by the tunicate cellulose nanocrystal matrix, allows it to be implanted through the pia mater without buckling [54, 55]. Once in the brain, the material is exposed to physiological heat (37 °C), raising the material above the glass transition temperature [51]. Additionally, the water molecules in the tissue displace hydrogen bonds holding the tunicate cellulose nanocrystal matrix together. In combination, the water and physiological heat cause the material to swell and become compliant, resulting in a lower Young's modulus of 10 MPa, reducing mechanical mismatch between the probe and brain tissue. Resveratrol can then elute from the material into the surrounding brain tissue, scavenging reactive oxygen species and exhibiting neuroprotective properties. Graphic created with BioRender.com.

the bottom for planarization. The dish was then covered with aluminum foil with venting holes to prevent any debris from entering, and placed in a vacuum oven (Isotemp Vacuum Oven Model 280 A, Fisher Scientific, Waltham, MA, USA) at 70 °C for one week to evaporate the DMF. After day 7, the dishes were removed from the oven, and the films were carefully removed from the dish with tweezers. The films were then stored in a dry box.

2.2. Material planarization

Although a layer of PDMS is used for planarization during the casting process, inherent material roughness from the cellulose nanocrystals and drying process prevents consistent photolithographic patterning of electrodes. To further reduce surface roughness, the material was pressed between two PDMS-coated acrylic discs in a Carver laboratory press. Acrylic discs with a diameter of 100 mm were cut from 1.6 mm-thick acrylic using a CO_2 laser (Versalaser, Universal Laser Systems, Scottsdale, AZ, USA). PDMS was spin-cast onto the acrylic disc to a thickness of approximately 50 μm using a spin-coater (Laurell Technologies, Lansdale, PA, USA). The polymer-based NC film with or without resveratrol was then trimmed to 100 mm-diameter and placed between two

PDMS-coated acrylic discs on a Carver Laboratory press for 15 min at 90 °C and 3000 psi. After pressing, the discs and film were allowed to cool completely before separating to prevent stretching or deformation. To ensure that the NC surface was sufficiently smooth for photolithographic patterning (roughness average less than 5000 Å), the surface roughness was measured at 3 different locations on each film using a Dektak stylus profilometer (Bruker, Billerica, MA, USA).

2.3. Resveratrol release measurements

The resveratrol release rate from the NC films was characterized using UV-vis spectrophotometry. The film was laser-micromachined into 3 cm × 0.6 cm strips, either in a rectangular (low laser path density) or serpentine (high laser path density) shape. Serpentine cut dimensions are denoted by the space in between each cut. After, the NC film strip was placed on a hot plate to bring it above its glass transition temperature, where it softened and was shaped into a helix. The helix shape allowed the entire NC film strip to be submerged in the incubation solution. Next, the NC film strip was weighed to determine the theoretical initial resveratrol content. The NC film strip was then incubated in 0.2 ml of 1X PBS in an Eppendorf tube and placed in a water bath at 37 °C until the
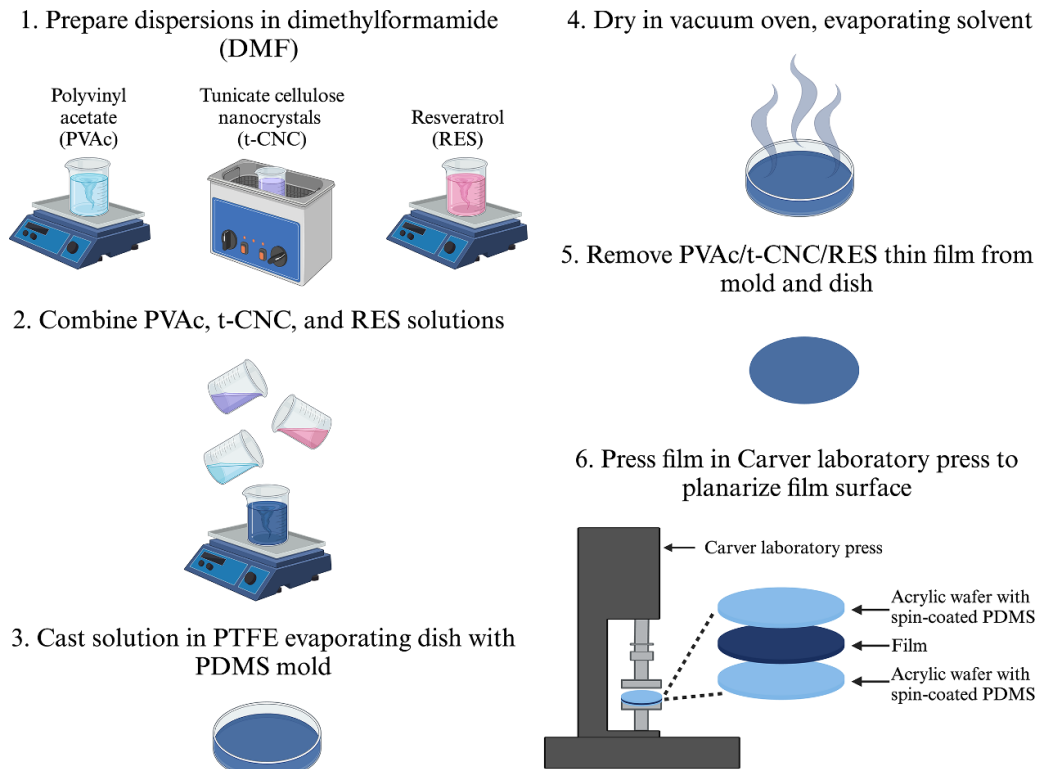
1. Prepare dispersions in dimethylformamide (DMF)

Polyvinyl acetate (PVAc)   Tunicate cellulose nanocrystals (t-CNC)   Resveratrol (RES)

2. Combine PVAc, t-CNC, and RES solutions

3. Cast solution in PTFE evaporating dish with PDMS mold

4. Dry in vacuum oven, evaporating solvent

5. Remove PVAc/t-CNC/RES thin film from mold and dish

6. Press film in Carver laboratory press to planarize film surface

← Carver laboratory press

Acrylic wafer with spin-coated PDMS
← Film
Acrylic wafer with spin-coated PDMS

Figure 2. Material dispersion, casting, and planarization process to create substrate for neural probes. Graphic created with BioRender.com.

designated time point. At the time point, 2 μl of the incubation solution was taken and measured with UV-vis spectrophotometry using a Nanodrop One (Thermo Fisher Scientific, Waltham, MA, USA). Absorbance spectra from 190 nm to 1050 nm were recorded. Following measurement, the sample was removed from the original Eppendorf tube, placed in a new tube, and filled with fresh 1X PBS, following an infinite sink drug release model. The incubation, measurment, and replacement steps were repeated for each timepoint.

Several different resveratrol release experiments were completed to determine the effect of loading concentration, laser-micromachining power, and laser-micromachining path density on release rate and profile. Similar steps for substrate preparation and release measurements were taken as described previously. Two different resveratrol loading concentrations, 0.01% w/w and 1% w/w were used to create polymer-only films for release studies. In addition, the release rate of PVAc loaded with 1% w/w resveratrol was evaluated to determine if the laser-micromachining path density affects release rate and absorbance spectra. Finally, laser-micromachining parameters of laser power and laser path density were investigated in an orthogonal experiment design to determine if laser-micromachining affects the resveratrol release profile and absorbance spectra.

2.4. Recording NC neural probe fabrication

After the NC was pressed and its surface roughness verified, electrode fabrication proceeded as detailed in figure 3. Parylene C was deposited using a SCS PDS 2010 Parylene Coater (Specialty Coating Systems, Indianapolis, IN, USA). The NC was mounted such that it was elevated above the stage so that the Parylene C film conformally coated all sides of the NC film during a single run. After Parylene C deposition, the NC film was then mounted to a carrier wafer by securing the edge with Kapton tape. Next, a 20 nm-thick titanium adhesion layer and a 200 nm-thick gold conductive layer were sputter-deposited on the substrate using a Denton Vacuum Explorer 14 deposition system (Denton Vacuum, Moorestown, NJ, USA). To pattern the metal, AZ P4330 photoresist (EMD Performance Materials, Darmstadt, Germany) was spin-cast on the wafer at 500 rpm for 10 s followed by 3000 rpm for 30 s. After a soft bake at 110 °C for 60 s on a hot plate, the wafer was exposed to i-line UV light in a photomask aligner (Karl Suss MA6, Suss Microtec, Garching, Germany) in hard contact mode with an exposure dose of 104 mJ cm^{-2}. The photoresist was then immersion-developed in AZ 400 K 1:4 developer (EMD Performance Materials, Darmstadt, Germany) for 2 min and rinsed in deionized water. The Au and Ti films were etched through the photoresist mask with Au etchant TFA (Transene Company Inc., Danvers, MA, USA) for 50 s and buffered oxide etchant (Transene Company Inc., Danvers, MA, USA) for 20 s, respectively. Next, a second 2 μm-thick Parylene C insulation layer was vapor-deposited on the metal layer. To pattern the Parylene C insulation layer, AZ nLOF 2070 photoresist (EMD Performance Materials, Darmstadt, Germany) was spin-cast onto the wafer at 200 rpm for 10 s followed by 3000 rpm for 30 s. The photoresist was soft baked at 110 °C for 90 s on a hot plate. The wafer was exposed in a mask aligner with an exposure dose of 176 mJ cm^{-2} in hard
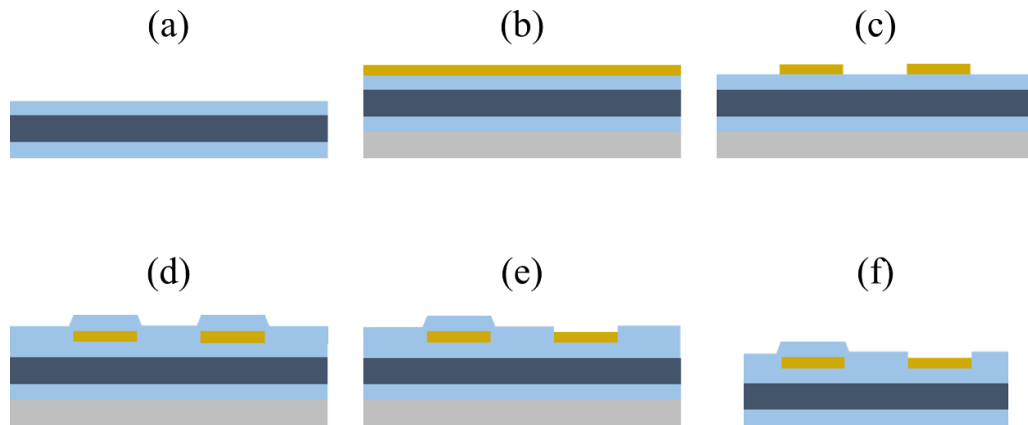
Figure 3. Microfabrication process to integrate recording electrodes on the PVAc/t-CNC/RES substrate. The procedure is described as follows: (a) a 2-μm thick Parylene C layer is vapor-deposited on both sides of the substrate. (b) The film is then mounted to a SiO$_2$ carrier wafer, and a Ti adhesion layer and Au conductive layer are sputter-deposited onto the substrate. (c) The metal is photolithographically patterned to create the electrode contacts and traces; excess metal is wet-etched. (d) A second Parylene C insulation layer is vapor-deposited on top of the patterned metal. (e) The Parylene C insulation layer is photolithographically patterned to expose recording and connector contacts using oxygen plasma. (f) Individual probes are laser-micromachined and released from the carrier wafer.

contact mode, and followed by a post-exposure bake at 110 °C for 90 s on a hot plate. Following the post-exposure bake, the photoresist was immersion-developed in 300 MIF developer (EMD Performance Materials, Darmstadt, Germany) for 2 min and rinsed with deionized water. The Parylene C was then etched with oxygen plasma in a MARCH CS 1701 plasma tool at a power of 200 W in an environment composed of 85% O$_2$ and 15% CF$_4$ to expose recording and connector contacts. Following plasma etching, individual probes were laser-micromachined using a picosecond laser micomachining tool (Oxford Lasers, Oxfordshire, UK) and released from the wafer. A completed mechanically-adaptive, reseveratrol-loaded neural probe with recording microelectrodes is shown in figure 4(a).

2.5. Device packaging

The neural probes were packaged to interface with external electronics for *in vivo* neural recoding and electrochemical impedance spectroscopy measurements, shown in figure 4(b). To prepare the package, connectors (DF30FC-20DS-0.4V(82), Hirose, Downers Grove, IL, USA) were soldered on both sides of a custom-made printed circuit board (PCB) (Advanced Circuits, Aurora, CO, USA). Ground and reference wires were soldered onto their respective contact pads. Next, the probe was secured to the PCB by placing a drop of cyanoacrylate adhesive and then aligning the connector contacts on the probe to the contact pads on the board. After drying, a silver-based conductive epoxy (8330-19G, MG Chemicals, Burlington, Ontario, Canada) was used to connect each of the 8 connector contacts to their respective contact pad, then cured at 65 °C for 2 h. To insulate the electrical connections, an insulating epoxy (EP21LVMed, Masterbond, Hackensack, New Jersey, USA) was applied over any electrically-conductive component of the PCB. The insulating epoxy was then left to cure for 2 d at room temperature, followed by 2 h at 80 °C, per the manufacturer's instructions.
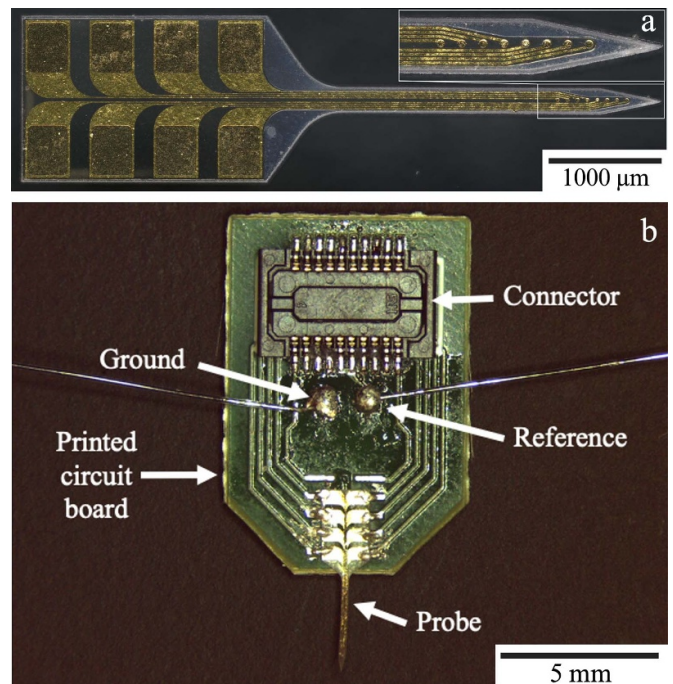

Figure 4. (a) Image of a mechanically-adaptive, resveratrol-eluting neural probe with fabricated recording electrodes. The inset shows the 8 recording contacts. (b) Device package for MARE probe. A Hirose connector, as well as ground and reference wires are soldered to the PCB.

2.6. Electrochemical impedance spectroscopy

Devices were tested for impedance prior to implantation to ensure their impedance was suitable for extracellular neural recording. A 3-electrode configuration was used. An Ag/AgCl reference electrode (BASi, West Lafayette, IN), a platinum mesh counter electrode and the probe shank were submerged into a 1X PBS solution. The probe was connected using a ZIF clip headstage to the Hirose connector, which then leads to a

breakout board where individual channels can be selected for testing. The electrodes were connected to a BioLogic SP-300 potentiostat (BioLogic, Seyssinet-Pariset, France) and a frequency sweep ranging from 1 Hz to 100 kHz was employed at an amplitude of 10 mV. Each channel is deemed acceptable for neural recording if its magnitude at 1 kHz is between 100–1000 kΩ [10, 20, 56–58]. Parameters for a Randels equivalent model were determined by fitting to the EIS data using the Zfit function in EC-lab (BioLogic, Seyssinet-Pariset, France) to understand the electrode's behavior.

2.7. In vivo *implantation surgeries*

Devices were implanted in male Sprague-Dawley rats 250–300 g in weight following established protocols [18, 59, 60] approved by the L. Stokes Cleveland Department of Veterans Affairs Medical Center. Each rat ($N = 5$) was implanted with a MARE probe. Rats were anethesized with 2.5% isoflurane gas. Once anestheized, the head was shaved and eye lubricant was applied. Each rat was administered a dose of the anaglesic meloxicam (1 mg kg^{-1}), the antibiotic cefazolin (16 mg kg^{-1}), and the local analgesic marcaine (0.15 ml of 0.25%). The animal was then placed on a stereotaxic frame with 2.0% isoflurane and the surgical site was scrubbed with betadine and isoproponal. While under anesthesia, the animals' vitals were being monitored with a MouseSTAT Pulse Oximeter and Heart Rate Monitor (Kent Scientific Corp., Torrington, CT, USA). An incision was made on the top of the head and the periosteum was removed to expose the skull. Hydrogen peroxide and VetBond (3M, St. Paul, MN, USA) were applied for skull dehydration and surface conditioning, respectively. Next, using a Kopf dental drill and a 1.35 mm drill bit (David Kopf Instruments, Tujunga, CA, USA) craniotomies for the ground and reference bone screws were made. The craniotomy for the ground bone screw was made at 1.5 mm lateral and 1.5 mm posterior to bregma and the craniotomy for the reference bone screw was made at 1.5 mm lateral and 5.5 mm posterior to bregma. For the craniotomy at the electrode implantation site, 3 mm lateral and 2 mm anterior to bregma on the contralateral side of the skull as the bone screws, a 1.75 mm drill bit was used. Drilling techinque for all craniotomies involved pulsing the drill and applying saline to reduce thermal damage and inflammation [61, 62]. Bone screws were placed using a screwdriver (Stoelting, Wood Dale, IL, USA). After the electrode was lowered near the craniotomy, the reference and ground wires were wrapped around their respective bone screws and dental cement (A-M Systems, Sequim, WA, USA) was applied to hold them in place. The electrode was then implanted using a hydraulic inserter (Model 2650, David Kopf Instruments, Tujunga, CA, USA) 2 mm into the cortex at a speed of 1 mm s^{-1}. After implantation, the surrounding craniotomy around the electrode was sealed with Kwik-Cast (World Precision Instruments, Sarasota, FL, USA). Dental cement was then layered around the skull to secure the electrode and screws in place as well as insulate the electrical connections. The incision was sutured around the headcap to allow access to the connector on the electrode. 2 doses of cefazolin (16 mg kg^{-1}) were given 1 d after surgery. 1 dose of meloxicam (1 mg kg^{-1}) was given on day 1 and another on day 2 post-operation.

2.8. In vivo *neural recording*

Neural recording sessions were done to evaluate recording performance from the MARE probes, following established protocols [63–65]. Animals were anesthesized with 2.5% isoflurane gas, and the exposed connector was then cleaned with isopropanol. Animals were placed in custom-made acrylic recording chamber. A ZC-16 ZIF-Clip headstage was clipped into both sides of the connector, which led to the ACO32 Commutator to help reduce motion artifacts and RA16PA 16 Channel Medusa Pre-Amp to filter the signal. The RZ5 Bioamp Processor (Tucker-Davis Technologies, Alachua, FL, USA) then processed the signal and displayed it in the Synapse software. After the animal woke up, the 10 min recording session began. A sampling rate of 24 414.1 Hz and a bandpass filter from 300–3000 Hz was used. After 10 min, the recording was stopped, the animal was released from the headstage, and returned to its home cage.

3. Results and discussion

3.1. Resveratrol-loaded polymer films are capable of slow, controlled release

The effect of resveratrol concentration in the polymer on release characteristics was determined by measuring the release profiles for rectangular polymer films loaded at 0.01% or 1% w/w resveratrol concentrations. Figure 5(a) shows a representative absorbance spectra from both films at the 1 h time point. There is a distinct peak at 306–317 nm [66–68], the wavelengths most strongly absorbed by trans-resveratrol, indicating that we are detecting the resveratrol released. The peak is much more pronounced for the PVAc-1% RES films, suggesting that the amount of reseveratrol released from the PVAc-0.01% RES films may be below the limit of the detection for our instrument. The large peak around 190 nm corresponds to hydrolysis of polvinyl acetate into polyvinyl alcohol. Figure 5(b) shows the cumulative resveratrol release profiles over 65 d in terms of resveratrol release in nanograms (ng) normalized to initial film weight in milligrams (mg). There is a fast initial release, with over 25% of the total resveratrol loading concentration released over the first 60 h, with slower release continuing thereafter over the entire 65 d, showing that the polymer is capable of slow, controlled release. Long-term release is more evident with PVAc-1% RES films, and the slow release at the amount released from PVAc-0.01% RES films at later time points is below the detection limit of our instrumentation. Although the lower percent weight films' release may be below the limit of detection in our detection system, the 0.01% wt concentration was shown to be optimal in microglial populations [33], and the release profile can be extrapolated to the lower concentration. The long-lasting, controlled resveratrol release is ideal for *in vivo* use, as the antioxidative and antiinflammatory properties of resveratrol may lessen chronic neuroinflammation [33, 69, 70].
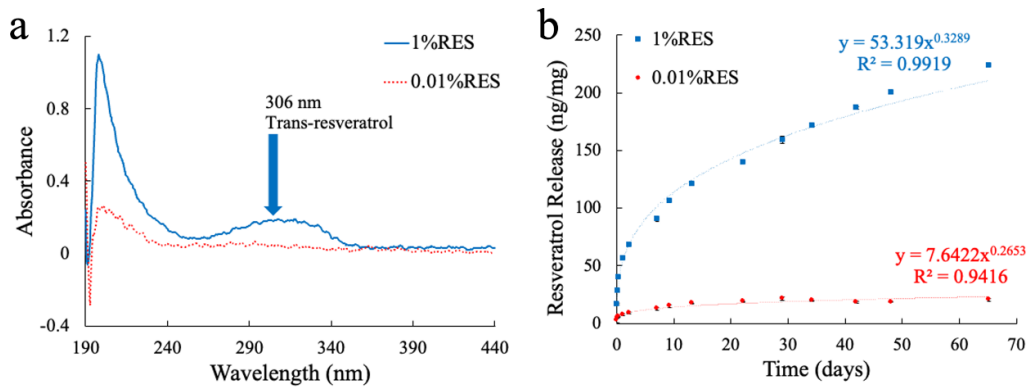
Figure 5. PVAc/RES release profile and absorbance spectra at 0.01% and 1% w/w loading concentrations. (a) Representative absorbance spectra from the 1-hour measurement from both sets of film. There is a distinct peak in the 1% RES between 306–317 nm, the wavelength at which trans-resveratrol absorbs. However, there is no visible peak with the 0.01% RES, indicating that the low resveratrol concentrations may be below the sensitivity limits of the Nanodrop One. (b) Release profiles of the 0.01% (red) and 1% (blue) resveratrol loading concentrations. They both follow a power release curve with low standard deviations between measurements. The 1% RES released a total of 200 ng mg^{-1} (ng of resveratrol per mg of initial film weight) of resveratrol over a 65-day time period, where the 0.01% appeared to release about 20 ng mg^{-1}.

3.2. Laser-micromachining path density affects resveratrol release from polymer films

PVAc-1% RES loaded polymer films were tested for resveratrol release profile with two different cut patterns—a rectangular shape and a serpentine shape with 200 μm between cuts, shown as R and Z-200 in figure 6. The serpentine shape greatly increased the laser-path density over the given area compared to the rectangular shape. The ratio of path length to rectangular sample area is 4.8 for the high laser path density shape, while it is 0.4 for the rectangular shape. Figure 7(b) shows the resveratrol release profile with the higher (serpentine) and lower (rectangular) laser-path densities, indicating that higher laser path density films exhibited faster resveratrol release normalized to initial film weight. Additionally, when looking at the absorbance spectra from both types of films in figure 7(a), there is a shift in wavelength among the serpentine films. The absorbance peaks from resveratrol released from the low laser path density films continued to be in the 306 nm–317 nm range, while the resveratrol from the high laser path density films exhibited a shift in peak to around 287 nm, corresponding to the peak absorption wavelength for cis-resveratrol absorbs. Cis-resveratrol is a less-therapeutic isomer of trans-resveratrol, which can undergo transformation when exposed to heat and UV light [66–68, 71–73]. The micromachining laser applies UV light ($\lambda = 355$ nm), which generates heat when cutting through the film. It is possible that the shift in absorbance wavelength corresponds with a conversion of trans-resveratrol to cis-resveratrol. These results indicate that while higher laser path density films will release resveratrol at a faster rate, the released resveratrol is likely the less potent cis- form of resveratrol compared to the lower laser path density films. The effect of laser path density on the polymer and resveratrol release profile is an important consideration to make for the fabrication process and the therapeutic level it may have *in vivo*. Laser path density is reduced for probes

patterned with recording electrodes by employing adequate spacing between devices on the film.

3.3. Laser-micromachining path density, but not laser power effects resveratrol release from polymer films

After determining that laser-path density had an effect on the resveratrol release profile and isomeric form of resveratrol, the interdependent effects of laser path density and laser power were studied in an orthogonal experiment design that examined the effects of both on the release profile and absorbance.

Table 1 shows the conditions tested in this study. Two different laser power levels, 5% (low, ~2 mW) and 55% (high ~22 mW) were tested, along with 4 different laser path density structures. The four test structures are as follows: (a) rectangular (low laser path density), (b) 1000 μm-wide serpentine (medium laser path density), (c) 200 μm-wide serpentine (high laser path density) and (d) 100 μm-wide serpentine (highest laser path density), shown in figure 6.

Figure 8(a) displays a reperesentative absorbance spectra from each condition. The higher laser path density samples showed a shift in peak absorbance to around 270 nm compared to the lower laser path density samples, which had peaks around 295 nm. The peak absorbances and wavelength at the peak absorbances are denoted in table 2, showing higher peak absorbances at lower wavelengths for high laser path density films. Together, our results suggests that both films release a mixture of trans- and cis- resveratrol, with the higher laser path density samples eluting more cis-resveratrol, similar to results from the previous experiment. The therapeutic efficacy is an important factor to consider when delivering resveratrol *in vivo*, as the amount independently may not completely explain the observed effect. Figure 8(b) shows the resveratrol release profile from all six conditions tested. The laser power
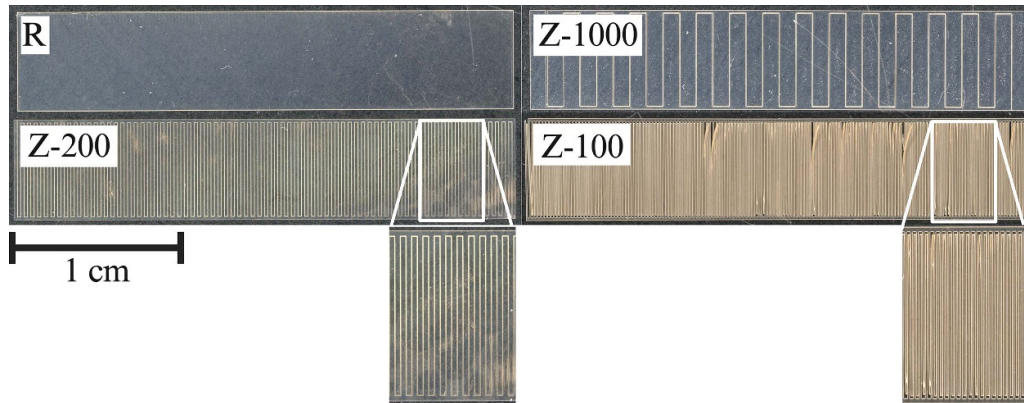
Figure 6. Test structures used to evaluate different laser path densities. The 'R' and 'Z-1000' structures have lower laser path densities, while the 'Z-200' and 'Z-100' structures have higher laser path densities. Graphic created with BioRender.com.
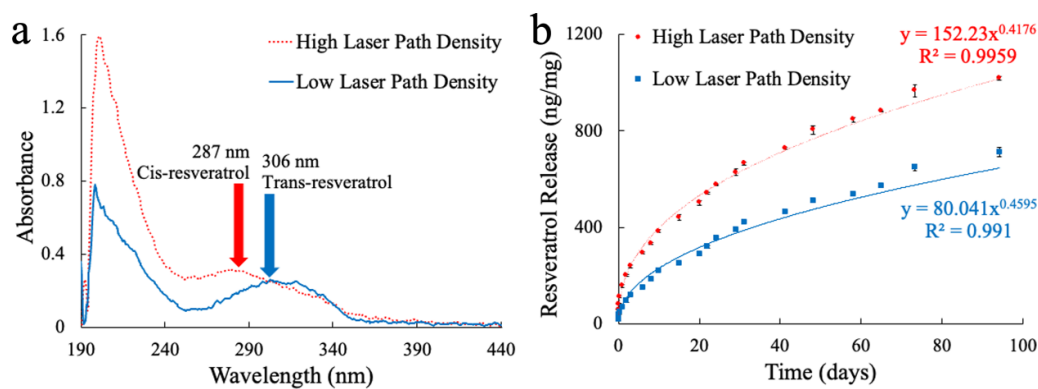

Figure 7. PVAc/1%RES release profile and absorbance spectra with different laser-micromachined shapes. The laser-micromachining tool was used to cut out both low laser path density and high laser path density shapes into the film, translating to different laser path densities over the same area of film. A rectangular shape of 3 cm × 0.6 cm was used for the low laser path density condition, while a 3 cm × 0.6 cm strip with 200 μm spaces between cuts is the high laser path density condition. (a) Representative absorbance spectra from low and high laser path density films. The low laser path density shape shows a characteristic peak at 306–317 nm, consistent with trans-resveratrol. However, the high laser path density shape shows an earlier peak around 287 nm, the wavelength at which the isomer cis-resveratrol absorbs. (b) Resveratrol release profile from low and high laser path density films. Both shapes followed a power release curve, with the low laser path density shape releasing resveratrol at a slower rate than the high laser path density shape.

Table 1. Laser power and laser path density structure combinations tested.

		Laser path density			
		R	Z-1000	Z-200	Z-100
Power	5%	X		X	
	55%	X	X	X	X

did not appear to impact the release rate, but the laser path density did, similar to the previous study. Higher laser path densities showed faster resveratrol release rates compared to lower laser path densities.

3.4. Electrochemical impedance spectroscopy

Electrochemical impedance spectroscopy was completed to determine if each channel on the MARE probes was suitable for neural recording of single units, with an impedance magnitude in the range of 100–1000 kΩ at 1 kHz. Figure 9

shows a representative impedance spectra from a MARE probe. Impedance spectropscopy spectrum show a magnitude that decreases with frequency, with the |Z| at 1 kHz in the suitable range for single unit neural recording. Additionally, the phase shows a frequency-dependent response similar to other Au electrodes [74–79], making this channel favorable for *in vivo* use. Further, the equivalent circuit characterizes the behavior of the electrode interface. The Randles circuit model with a constant phase element was fit to the EIS data, with R_s = 13.293 kΩ, representing the solution resistance, Q = 4.82 nF.s$^{(a-1)}$ representing the constant phase element, a = 0.8215, and R_{ct} = 507.9 MΩ representing the charge transfer resistance. Figure S1 shows the benchtop 1 kHz impedance magnitude |Z| of all 8 channels from a representative MARE probe. Additionally, figure S2 displays the benchtop |Z| from the same channel, channel 2, across all of the MARE probes used for *in vivo* studies. Combined, the figures indicate that the MARE probes have repeatable and consistent electrical properties, with impedances at 1 kHz in the range of 100–1000 kΩ, suitable for recording single units.
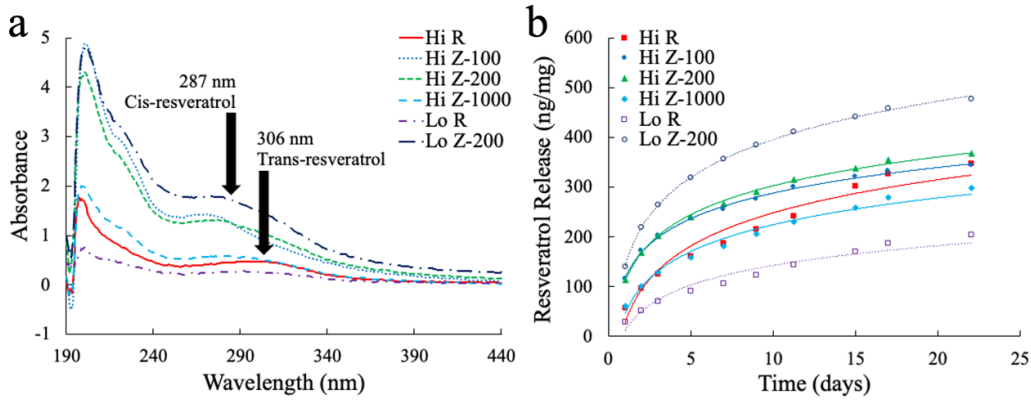
Figure 8. Resveratrol release profile and absorbance spectra for different laser-micromachining path density and laser power with PVAc/1%RES films. Six different combinations of laser path density and power were tested. 'Hi' is high laser power and 'Lo' is low laser power. Laser path density is the lowest in the 'R' structures and increases in this order: 'Z-1000', 'Z-200', and 'Z-100'. (a) Representative absorbance spectra for six different conditions tested. Similar to figure 6, higher laser path density film samples had a shift in peak absorbance to around 270 nm, suggesting that cis-resveratrol is being released from the substrate. Lower-laser path density samples still observed a slight shift in peak absorbance, suggesting there is both trans-and cis-resveratrol eluting from the substrate. (b) Overall, it appeared that laser power did not seem to impact the resveratrol release profile or release rate. However, the laser path density again impacted the resveratrol release rate, with higher laser path densities (Z-100 and Z-200) having faster release rates than lower laser path densities (Z-1000 and R).

Table 2. Peak absorbance and wavelength at peak absorbance values for the representative spectra shown in figure 8.

Film type	Peak absorbance (AU)	Wavelength at peak absorbance (nm)
Hi R	0.45	296
Hi Z-100	1.39	270
Hi Z-200	1.37	271
Hi Z-1000	0.57	282
Lo R	0.24	295
Lo Z-200	1.78	269

Probe functionality is an important consideration in this device design, as it was unknown if the resveratrol would interfere with the ability to fabricate probes with functional recording channels. Because the probes have a low laser path density when laser-micromachining, the fabrication of these functional recording devices circumvents the deleterious conversion of trans-resveratrol to cis-resveratrol.

3.5. In vivo *neural recording*

In vivo neural recording sessions demonstrated the MARE probe's ability to record single units *in vivo*. Comparing the benchtop and *in vivo* impedance spectra taken within hours after implantation, 92.5% electrodes survived, meaning their impedances at 1 kHz were within the 100–1000 kΩ range. Twice weekly recording sessions took place beginning on the day of surgery. The pile plots in figure 10 are from units recorded from the same channel on a MARE probe on day 32 (left) and day 34 (right). The peak-to-peak voltages are 56 μV and 54 μV, the mean interspike intervals are 374 ms and 165 ms, and the signal-to-noise ratios are 7.12 and 7.06 for
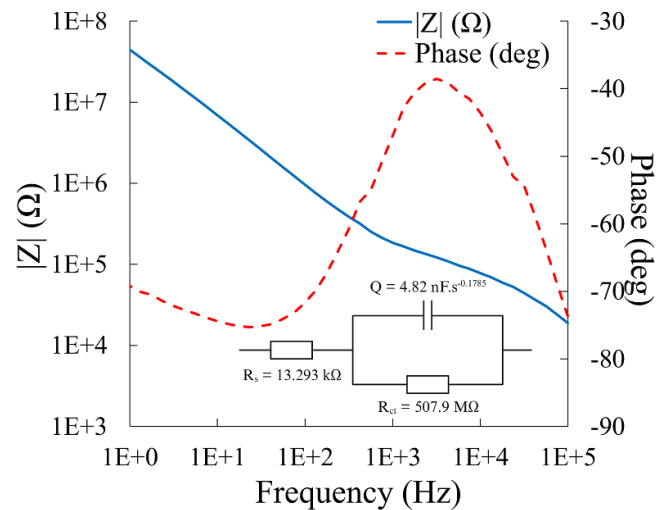

Figure 9. Representative electrochemical impedance spectroscopy with equivalent circuit from a MARE probe. A key metric is the impedance magnitude at 1 kHz, which should be between 100–1000 kΩ for viable recording electrodes. The magnitude and phase spectra show a frequency-dependent response similar to other Au electrodes.

each unit shown, respectively. The single unit metrics are similar between recording sessions indicating recording stability from the MARE probes. The ability to record single units with stability demonstrates that MARE probes are functional *in vivo,* which is a critical requirement for clinical translation or use in neuroscience research.

The current study marks the first instance of local resveratrol delivery from a NC-based probe combined with neural recording. Previously, resveratrol was incorporated into NC-based dummy probes. Additionally, NC-based probes without
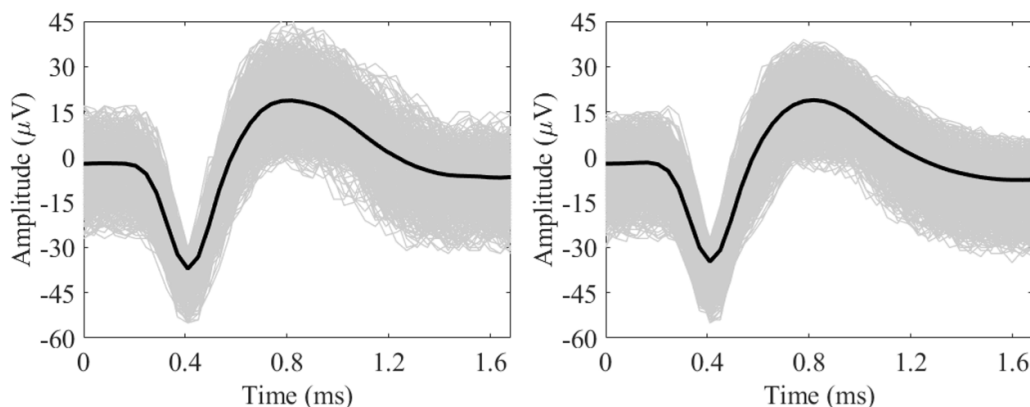
Figure 10. Pile plots of a single unit from the same channel on a MARE probe implanted *in vivo* during separate recording sessions on day 32 and day 34 post-implantation. The average waveform of the unit is in the thick black line, and the waveforms recorded are in gray. The amplitude, noise band, and waveform shape remain stable while implanted in the rat motor cortex.

recording capability have been integrated with microfluidic channels using soft lithography to deliver resveratrol at a chronic timepoint [59]. Overall, microfabrication techniques have improved the integration of drug delivery systems into implantable devices.

4. Conclusion

In this work, we have shown that the MARE neural probes can be successfully fabricated and implemented for chronic *in vivo* use. The mechanically-compliant, resveratrol-loaded substrate can be made through a dispersion, casting, and evaporation method. Functional electrodes can then be integrated onto the substrate using a specific microfabrication process to promote precise patterning and protection of the material. Benchtop EIS testing has shown that these electrodes have a 1 kHz impedance magnitude in the range suitable for neural recording. Additionally, MARE probes have been implanted *in vivo* and were capable of maintaining recording of single units for weeks post-implantation.

Resveratrol release studies indicate that the MARE probes are capable of long-term continuous release of resveratrol. However, we did discover that the fabrication process may contribute to degradation of the resveratrol. Specifically, high-density laser-micromachining seemed to play a role in the transformation of the loaded trans-resveratrol to its less potent isomer, cis-resveratrol. This is likely due to the UV light the laser applies to cut the substrate, and a consideration that needs to be made going forward with these substrates.

Overall, the MARE probes have been well-characterized in terms of fabrication process, resveratrol delivery, and electrode impedance. With their mechanically-compliant substrate and ability to locally delivery an antioxidant, MARE probes have the potential to reduce the neuroinflammatory response and improve IME recording performance compared to traditional silicon IMEs. The next step with these devices is to complete a comparative study *in vivo* with both MARE probes and silicon probes to evaluate the effects of stiffness and resveratrol release on IME integration and the stability of performance.

Data availability statement

The data cannot be made publicly available upon publication because the cost of preparing, depositing and hosting the data would be prohibitive within the terms of this research project. The data that support the findings of this study are available upon reasonable request from the authors.

Ethical statement

All animal procedures were completed following established protocols approved by the L Stokes Cleveland Department of Veterans Affairs Medical Center.

ORCID iDs

Natalie N Mueller ⬤ https://orcid.org/0000-0003-0336-3686
Jeffrey R Capadona ⬤ https://orcid.org/0000-0001-8030-6947
Allison Hess-Dunning ⬤ https://orcid.org/0000-0003-4060-1145

References

[1] Merritt C H, Taylor M A, Yelton C J and Ray S K 2019 Economic impact of traumatic spinal cord injuries in the United States *Neuroimmunol. Neuroinflammation* **6** 9

[2] Schoenfeld A J, Goodman G P and Belmont P J 2012 Characterization of combat-related spinal injuries sustained by a US army brigade combat team during operation Iraqi freedom *Spine J.* **12** 771–6

[3] Kowal S L, Dall T M, Chakrabarti R, Storm M V and Jain A 2013 The current and projected economic burden of Parkinson's disease in the United States *Mov. Disorders* **28** 311–8

[4] Ahuja C S, Wilson J R, Nori S, Kotter M R N, Druschel C, Curt A and Fehlings M G 2017 Traumatic spinal cord injury *Nat. Rev. Dis. Primers* **3** 17018

[5] Krueger C A, Wenke J C and Ficke J R 2012 Ten years at war: comprehensive analysis of amputation trends *J. Trauma Acute Care Surg.* **73** S438–44

[6] Daly J J and Wolpaw J R 2008 Brain–computer interfaces in neurological rehabilitation *Lancet Neurol* **7** 1032–43

[7] Chen R, Canales A and Anikeeva P 2017 Neural recording and modulation technologies *Nat. Rev. Mater.* **2** 16093

[8] Chestek C A *et al* 2011 Long-term stability of neural prosthetic control signals from silicon cortical arrays in rhesus macaque motor cortex *J. Neural Eng.* **8** 045005

[9] Barrese J C, Rao N, Paroo K, Triebwasser C, Vargas-Irwin C, Franquemont L and Donoghue J P 2013 Failure mode analysis of silicon-based intracortical microelectrode arrays in non-human primates *J. Neural Eng.* **10** 066014

[10] Prasad A and Sanchez J C 2012 Quantifying long-term microelectrode array functionality using chronic *in vivo* impedance testing *J. Neural Eng.* **9** 026028

[11] Usoro J O, Sturgill B S, Musselman K C, Capadona J R and Pancrazio J J 2021 Intracortical microelectrode array unit yield under chronic conditions: a comparative evaluation *Micromachines* **12** 972

[12] Kozai T D, Jaquins-Gerstl A S, Vazquez A L, Michael A C and Cui X T 2015 Brain tissue responses to neural implants impact signal sensitivity and intervention strategies *ACS Chem. Neurosci.* **6** 48–67

[13] Bennett C, Mohammed F, Álvarez-Ciara A, Nguyen M A, Dietrich W D, Rajguru S M, Streit W J and Prasad A 2019 Neuroinflammation, oxidative stress, and blood-brain barrier (BBB) disruption in acute Utah electrode array implants and the effect of deferoxamine as an iron chelator on acute foreign body response *Biomaterials* **188** 144–59

[14] Kozai T, Marzullo T C, Hooi F, Langhals N B, Majewska A K, Brown E B and Kipke D R 2010 Reduction of neurovascular damage resulting from microelectrode insertion into the cerebral cortex using *in vivo* two-photon mapping *J. Neural Eng.* **7** 046011

[15] Bjornsson C S, Oh S J, Al-Kofahi Y A, Lim Y J, Smith K L, Turner J N, De S, Roysam B, Shain W and Kim S J 2006 Effects of insertion conditions on tissue strain and vascular damage during neuroprosthetic device insertion *J. Neural Eng.* **3** 196–207

[16] Saxena T, Karumbaiah L, Gaupp E A, Patkar R, Patil K, Betancur M, Stanley G B and Bellamkonda R V 2013 The impact of chronic blood-brain barrier breach on intracortical electrode function *Biomaterials* **34** 4703–13

[17] Mendiola A S *et al* 2020 Transcriptional profiling and therapeutic targeting of oxidative stress in neuroinflammation *Nat. Immunol.* **21** 513–24

[18] Ereifej E S, Rial G M, Hermann J K, Smith C S, Meade S M, Rayyan J M, Chen K, Feng H and Capadona J R 2018 Implantation of neural probes in the brain elicits oxidative stress *Front. Bioeng. Biotechnol.* **6** 1–12

[19] Kaur U, Banerjee P, Bir A, Sinha M, Biswas A and Chakrabarti S 2015 Reactive oxygen species, redox signaling and neuroinflammation in Alzheimer's disease: the NF-kB connection *Curr. Top. Med. Chem.* **15** 446–57

[20] Prasad A, Xue Q-S, Sankar V, Nishida T, Shaw G, Streit W J and Sanchez J C 2012 Comprehensive characterization and failure modes of tungsten microwire arrays in chronic neural implants *J. Neural Eng.* **9** 056015

[21] Prasad A, Xue Q-S, Dieme R, Sankar V, Mayrand R C, Nishida T, Streit W J and Sanchez J C 2014 Abiotic-biotic characterization of Pt/Ir microelectrode arrays in chronic implants *Front. Neuroeng.* **7** 2

[22] Takmakov P, Ruda K, Phillips K S, Isayeva I S, Krauthamer V and Welle C G 2015 Rapid evaluation of the durability of cortical neural implants using accelerated aging with reactive oxygen species *J. Neural Eng.* **12** 026003

[23] Liu B, Gao H-M, Wang J-Y, Jeohn G-H, Cooper C L and Hong J-S 2002 Role of nitric oxide in inflammation-mediated neurodegeneration *Ann. New York Acad. Sci.* **962** 318–31

[24] Rehman S, Ikram M, Ullah N, Alam S, Park H, Badshah H, Choe K and Ok Kim M 2019 Neurological enhancement effects of melatonin against brain injury-induced oxidative stress, neuroinflammation, and neurodegeneration via AMPK/CREB signaling *Cells* **8** 760

[25] Salatino J W, Ludwig K A, Kozai T D Y and Purcell E K 2017 Glial responses to implanted electrodes in the brain *Nat. Biomed. Eng.* **1** 862–77

[26] Moshayedi P, Ng G, Kwok J C F, Yeo G S H, Bryant C E, Fawcett J W, Franze K and Guck J 2014 The relationship between glial cell mechanosensitivity and foreign body reactions in the central nervous system *Biomaterials* **35** 3919–25

[27] Stiller A, Black B, Kung C, Ashok A, Cogan S, Varner V and Pancrazio J 2018 A meta-analysis of intracortical device stiffness and its correlation with histological outcomes *Micromachines* **9** 443

[28] Gilletti A and Muthuswamy J 2006 Brain micromotion around implants in the rodent somatosensory cortex *J. Neural Eng.* **3** 189–95

[29] Rivnay J, Wang H, Fenno L, Deisseroth K and Malliaras G G 2017 Next-generation probes, particles, and proteins for neural interfacing *Sci. Adv.* **3** e1601649

[30] Ward M P, Rajdev P, Ellison C and Irazoqui P P 2009 Toward a comparison of microelectrodes for acute and chronic recordings *Brain Res.* **1282** 183–200

[31] Biran R, Martin D C and Tresco P A 2007 The brain tissue response to implanted silicon microelectrode arrays is increased when the device is tethered to the skull *J. Biomed. Mater. Res.* A **82** 169–78

[32] Huang J, Huang N, Xu S, Luo Y, Li Y, Jin H, Yu C, Shi J and Jin F 2021 Signaling mechanisms underlying inhibition of neuroinflammation by resveratrol in neurodegenerative diseases *J. Nutr. Biochem.* **88** 108552

[33] Nguyen J K, Jorfi M, Buchanan K L, Park D J, Foster E J, Tyler D J, Rowan S J, Weder C and Capadona J R 2016 Influence of resveratrol release on the tissue response to mechanically adaptive cortical implants *Acta Biomater.* **29** 81–93

[34] Potter K A, Jorfi M, Householder K T, Foster E J, Weder C and Capadona J R 2014 Curcumin-releasing mechanically-adaptive intracortical implants improve the proximal neuronal density and blood-brain barrier stability *Acta Biomater.* **10** 2209–22

[35] Potter K A, Buck A C, Self W K, Callanan M E, Sunil S and Capadona J R 2013 The effect of resveratrol on neurodegeneration and blood brain barrier stability surrounding intracortical microelectrodes *Biomaterials* **34** 7001–15

[36] Potter-Baker K A and Capadona J R 2015 Reducing the "Stress": antioxidative therapeutic and material approaches may prevent intracortical microelectrode failure *ACS Macro Lett.* **4** 275–9

[37] Potter-Baker K A, Nguyen J K, Kovach K M, Gitomer M M, Srail T W, Stewart W G, Skousen J L and Capadona J R 2014 Development of superoxide dismutase mimetic surfaces to reduce accumulation of reactive oxygen species surrounding intracortical microelectrodes *J. Mater. Chem.* B **2** 2248–58

[38] Potter-Baker K A, Stewart W G, Tomaszewski W H, Wong C T, Meador W D, Ziats N P and Capadona J R 2015 Implications of chronic daily anti-oxidant administration on the inflammatory response to intracortical microelectrodes *J. Neural Eng.* **12** 046002

[39] Chen R, Funnell J L, Quinones G B, Bentley M, Capadona J R, Gilbert R J and Palermo E F 2023 Poly(pro-curcumin) materials exhibit dual release rates and prolonged antioxidant activity as thin films and self-assembled particles *Biomacromolecules* **24** 294–307

[40] Ziemba A M *et al* 2023 Development of a slow-degrading polymerized curcumin coating for intracortical microelectrodes *ACS Appl. Bio Mater.* **6** 806–18

[41] Nguyen J K, Park D J, Skousen J L, Hess-Dunning A E, Tyler D J, Rowan S J, Weder C and Capadona J R 2014 Mechanically-compliant intracortical implants reduce the neuroinflammatory response *J. Neural Eng.* **11** 056014

[42] Harris J, Capadona J R, Miller R H, Healy B C, Shanmuganathan K, Rowan S J, Weder C and Tyler D J 2011 Mechanically adaptive intracortical implants improve the proximity of neuronal cell bodies *J. Neural Eng.* **8** 066011

[43] Stiller A *et al* 2018 Chronic intracortical recording and electrochemical stability of thiol-ene/acrylate shape memory polymer electrode arrays *Micromachines* **9** 500

[44] Koch B, Rubino I, Quan F-S, Yoo B and Choi H-J 2016 Microfabrication for drug delivery *Materials* **9** 646

[45] Pons-Faudoa F P, Ballerini A, Sakamoto J and Grattoni A 2019 Advanced implantable drug delivery technologies: transforming the clinical landscape of therapeutics for chronic diseases *Biomed. Microdevices* **21** 1–22

[46] Tran K T M and Nguyen T D 2023 Lithography in drug delivery *Nano- and Microfabrication Techniques in Drug Delivery: Recent Developments and Future Prospects* ed D Lamprou (Springer) pp 249–74

[47] Wise K D and Najafi K 1991 Microfabrication techniques for integrated sensors and microsystems *Science* **254** 1335

[48] FitzGerald J J 2016 Suppression of scarring in peripheral nerve implants by drug elution *J. Neural Eng.* **13** 026006

[49] Barone D G *et al* 2022 Prevention of the foreign body response to implantable medical devices by inflammasome inhibition *Proc. Natl Acad. Sci.* **119** e2115857119

[50] van den Berg O, Capadona J R and Weder C 2007 Preparation of homogeneous dispersions of tunicate cellulose whiskers in organic solvents *Biomacromolecules* **8** 1353–7

[51] Capadona J R, Shanmuganathan K, Tyler D J, Rowan S J and Weder C 2008 Stimuli-responsive polymer nanocomposites inspired by the sea cucumber dermis *Science* **319** 1370–4

[52] Shanmuganathan K, Capadona J R, Rowan S J and Weder C 2010 Stimuli-responsive mechanically adaptive polymer nanocomposites *ACS Appl. Mater. Interfaces* **2** 165–74

[53] Shanmuganathan K, Capadona J R, Rowan S J and Weder C 2010 Biomimetic mechanically adaptive nanocomposites *Prog. Polym. Sci.* **35** 212–22

[54] Harris J, Hess A E, Rowan S J, Weder C, Zorman C A, Tyler D J and Capadona J R 2011 *In vivo* deployment of mechanically adaptive nanocomposites for intracortical microelectrodes *J. Neural Eng.* **8** 046010

[55] Hess-Dunning A and Tyler D 2018 A mechanically-adaptive polymer nanocomposite-based intracortical probe and package for chronic neural recording *Micromachines* **9** 583

[56] Suner S, Fellows M R, Vargas-Irwin C, Nakata G K and Donoghue J P 2005 Reliability of signals from a chronically implanted, silicon-based electrode array in non-human primate primary motor cortex *IEEE Trans. Rehabil. Eng.* **13** 524–41

[57] Vetter R J, Williams J C, Hetke J F, Nunamaker E A and Kipke D R 2004 Chronic neural recording using silicon-substrate microelectrode arrays implanted in cerebral cortex *IEEE Trans. Biomed. Eng.* **51** 896–904

[58] Jiang J, Willett F R and Taylor D M 2014 Relationship between microelectrode array impedance and chronic recording quality of single units and local field potentials *2014 36th Annual Int. Conf. IEEE Engineering in Medicine and Biology Society* (*1 August 2014*) (IEEE) (https://doi.org/10.1109/embc.2014.6944265)

[59] Kim Y, Mueller N N, Schwartzman W E, Sarno D, Wynder R, Hoeferlin G F, Gisser K, Capadona J R and Hess-Dunning A 2023 Fabrication methods and chronic *in vivo* validation of mechanically adaptive microfluidic intracortical devices *Micromachines* **14** 1015

[60] Mahajan S *et al* 2020 Toward standardization of electrophysiology and computational tissue strain in rodent intracortical microelectrode models *Front. Bioeng. Biotechnol.* **8** 416

[61] Shoffstall A J, Paiz J E, Miller D M, Rial G M, Willis M T, Menendez D M, Hostler S R and Capadona J R 2018 Potential for thermal damage to the blood-brain barrier during craniotomy: implications for intracortical recording microelectrodes *J. Neural Eng.* **15** 034001

[62] Capadona J R, Shoffstall A J, Krebs O K, Hoeferlin G F and Menendez D M 2022 Assessment of thermal damage from robot-drilled craniotomy for cranial window surgery in mice *J. Vis. Exp.* **189** e64188

[63] Hoeferlin G F *et al* 2023 Antioxidant dimethyl fumarate temporarily but not chronically improves intracortical microelectrode performance *Micromachines* **14** 1902

[64] Ereifej E S *et al* 2020 Investigating the association between motor function, neuroinflammation, and recording metrics in the performance of intracortical microelectrode implanted in motor cortex *Micromachines* **11** 838

[65] Kim Y *et al* 2021 Investigation of the feasibility of ventricular delivery of resveratrol to the microelectrode tissue interface *Micromachines* **12** 1446

[66] Nour V, Trandafir I and Muntean C 2012 Ultraviolet irradiation of trans-resveratrol and HPLC determination of trans-resveratrol and cis-resveratrol in romanian red wines *J. Chromatogr. Sci.* **50** 920–7

[67] Trela B C and Waterhouse A L 1996 Resveratrol: isomeric molar absorptivities and stability *J. Agric. Food Chem.* **44** 1253–7

[68] Allan K E, Lenehan C E and Ellis A V 2009 UV light stability of α-cyclodextrin/resveratrol host—Guest complexes and isomer stability at varying pH *Aust. J. Chem.* **62** 921

[69] Ates O, Cayli S, Altinoz E, Gurses I, Yucel N, Sener M, Kocak A and Yologlu S 2007 Neuroprotection by resveratrol against traumatic brain injury in rats *Mol. Cell. Biochem.* **294** 137–44

[70] Schlotterose L, Pravdivtseva M S, Ellermann F, Jansen O, Hövener J-B, Sönnichsen F D, Cossais F, Lucius R and Hattermann K 2023 Resveratrol mitigates metabolism in human microglia cells *Antioxidants* **12** 1248

[71] Dutta S, Mahalanobish S and Sil P C 2021 Phytoestrogens as novel therapeutic molecules against breast cancer *Discovery and Development of Anti-Breast Cancer Agents from Natural Products* ed G Brahmachari (Elsevier) ch 8, pp 197–229

[72] López-Hernández J, Paseiro-Losada P, Sanches-Silva A T and Lage-Yusty M A 2007 Study of the changes of trans-resveratrol caused by ultraviolet light and determination of trans- and cis-resveratrol in Spanish white wines *Eur. Food Res. Technol.* **225** 789–96

[73] Mattioli R *et al* 2022 Effect of natural deep eutectic solvents on trans-resveratrol photo-chemical induced isomerization and 2,4,6-trihydroxyphenanthrene electro-cyclic formation *Molecules* **27** 2348

[74] Kremers T, Menzel N, Freitag F, Laaf D, Heine V, Elling L and Schnakenberg U 2020 Electrochemical impedance spectroscopy using interdigitated gold–polypyrrole electrode combination *Phys. Status Solidi* a **217** 1900827

[75] Rocha P R F, Schlett P, Kintzel U, Mailänder V, Vandamme L K J, Zeck G, Gomes H L, Biscarini F and de Leeuw D M 2016 Electrochemical noise and impedance of Au electrode/electrolyte interfaces enabling extracellular detection of glioma cell populations *Sci. Rep.* **6** 34843

[76] Kim J, Jeong H S, Jun S B and Seo J-M 2023 Implantable neural electrodes fabrication based on perfluoroalkoxyalkane film *IEEE Trans. Biomed. Eng.* **71** 1–11

[77] Cui X and Martin D C 2003 Fuzzy gold electrodes for lowering impedance and improving adhesion with electrodeposited conducting polymer films *Sens. Actuators* A **103** 384–94

[78] Hess A E and Zorman C A 2011 Fabrication and characterization of MEMS-based structures from a bio-inspired, chemo-responsive polymer nanocomposite *MRS Online Proc. Lib.* **1299** 407

[79] Wise K D and Angell J B 1975 A low-capacitance multielectrode probe for use in extracellular neurophysiology *IEEE Trans. Biomed. Eng.* **BME-22** 212–9